# DC–AC Talkative Power Conversion Based on Variable Zero-Vector Position Modulation

Yang Leng, *Student Member, IEEE*, Rongwu Zhu, *Senior Member, IEEE*, Peter Adam Hoeher, *Fellow, IEEE*, and Marco Liserre, *Fellow, IEEE*

***Abstract*—Talkative power conversion (TPC), which embeds information in the switching ripple to achieve simultaneous power and data transmission without installing any or few additional hardware at the transmitter side, can reduce the additional communication infrastructure needed in cyber-physical systems like smart grids and renewable power plants. While in dc–dc converters TPC has been the subject of numerous investigations, dc–ac converters have received less attention. Recently, zero vectors of three-phase dc–ac converters were used to embed data, and variable zero vector width modulation TPC has been investigated. In this study, a novel zero vector-based modulation, called variable zero-vector position modulation, is proposed for three-phase dc–ac TPC with improved communication performance. This type of dc–ac converter can send data through the power line to the demodulator with good power quality. The viability of using sliding fast fourier transform (FFT)-based demodulation for target side-band harmonics is supported by a mathematical study of the harmonic distribution. The results of MATLAB/Simulink-based simulations and scaled-down prototype-based experimental results verify the correctness of the theoretical analysis. Besides, the bit error rate is evaluated for different line lengths and zero vector positions.**

***Index Terms*—Space vector pulsewidth modulation (PWM) (SVPWM), talkative power conversion (TPC), three-phase dc–ac converter, variable zero vector position modulation (VZVPM).**

## I. INTRODUCTION

As a result of the increasing penetration of renewable energy sources into smart grids with power converter interfaces, numerous communication infrastructures have been created to monitor renewable energy sources and regulate grid-connected power converters to achieve system-level control.

Both wired and wireless communication infrastructures are used in smart grids, such as WiMax, fiber, cellular radio, ZigBee, and home access networking [1]. Because expenses associated with setting up and maintaining channels rise, smart grids have made extensive use of power line communication (PLC), especially in tertiary control, which sends data by injecting modulated carriers into power buses without the need for independent data wires. However, traditional PLC needs couplers to inject/extract data, and there may be stability and safety issues with the injected information-carrying signals [2].

A PLC technique with zero-additional or few-additional hardware at the transmitter side has been proposed in [3], where power and data can be delivered simultaneously without couplers. This technology was dubbed talkative power (targeting the physical layer of communication-enhanced power conversion using ripple modulation) in [4], power-talk (targeting system control of networked power converters by communication signal injection in the control loop) in [4] and [5], and talkative power conversion (TPC) (considering all layers of the open system interconnection (OSI) reference model) in [6]. TPC is an excellent replacement of conventional PLC for scenarios with high penetration of power electronics-interfaced resources. According to the modulation technique, TPC can be broadly classified as reference signal-based TPC (RS-TPC) and carrier signal-based TPC (CS-TPC). In RS-TPC, modulated signals are superimposed onto the reference signal [7], [8], [9], while in CS-TPC, the pulsewidth modulation (PWM) carriers are reshaped. The superposition causes the reference voltage in RS-TPC to jitter, which can cause instability. According to the degrees of freedom of the PWM carriers [10], frequency-shift keying (FSK) [11], phase-shift keying (PSK), pulse position modulation, and combinations thereof can be exploited for CS-TPC [12]. Various TPC technologies have been comprehensively reviewed in [6]. However, most TPC research has been done regarding dc–dc converters.

The use of dc–ac TPC is attractive because of the widespread use of modern ac power systems. Recently, a number of researchers have begun to focus on RS-TPC and CS-TPC in dc–ac converters. For single-phase dc–ac TPC, data are mostly modulated on the reference loop based on PSK and FSK [13], [14]. There are few references to CS-TPC in dc–ac inverters. However, the most common dc–ac inverter used in smart grids is the three-phase dc–ac inverter, which could be the focus of TPC research in ac smart grids.

---

Received 24 September 2024; revised 16 January 2025; accepted 7 February 2025. Date of publication 11 February 2025; date of current version 20 March 2025. This work was supported in part by the National Natural Science Foundation of China under Grant 52377174, in part by the Foreign Expert Project under Grant S20240024, in part by the Guangdong Provincial Natural Science Foundation under Grant 2023A1515011254, in part by the Talent Recruitment Project of Guangdong under Grant 2021QN02L474, in part by the Special Major Program on Science and Technology of Xinjiang Autonomous Region under Grant 2022A01007, and in part by the Major project of Natural Science Foundation of Shenzhen-the Stable Support Plan Program under Grant GXWD20220819112051004. Recommended for publication by Associate Editor D. O Neacsu. *(Corresponding author: Rongwu Zhu.)*

Yang Leng and Rongwu Zhu are with the Department of Electrical Engineering, Harbin Institute of Technology, Shenzhen 518055, China (e-mail: 24B353018@stu.hit.edu.cn; rzh@hit.edu.cn).

Peter Adam Hoeher is with the Chair of Information and Coding Theory, Kiel University, 24143 Kiel, Germany (e-mail: ph@tf.uni-kiel.de).

Marco Liserre is with the Chair of Power Electronics, Kiel University, 24143 Kiel, Germany (e-mail: ml@tf.uni-kiel.de).

Color versions of one or more figures in this article are available at https://doi.org/10.1109/TPEL.2025.3541040.

Digital Object Identifier 10.1109/TPEL.2025.3541040

TABLE I
Comparison Between the Proposed VZVPM and Other Three-Phase DC–AC TPC Approaches

| **Refs** | **Methods** | **PWM type** | **Bit rate** | **BER** | **Close-loop** | **Switching frequency** | **$\Delta$THD** | **Average switching times** | **PLL** | **Latency** |
|---|---|---|---|---|---|---|---|---|---|---|
| [15] | RS-TPC-FSK | SPWM | 0–100 b/s | / | Needed | 1, 2 kHz | High | 1 ON-OFF/Period | Needed | 6 ms |
| [16] | CS-TPC-FSK | Phase-disposition SPWM | 0–600 b/s | Low | Not needed | 2, 4, 6, 8, 10 kHz | High | 1 ON-OFF/Period | Not needed | 4.2 ms |
| [17] | RS-TPC-ASK (ON-OFF-Keying) | SPWM | 0–1000 b/s | / | Needed | 10 kHz | High | 1 ON-OFF/Period | Needed | 20–100 ms |
| [18] | CS-TPC-PSK | SPWM | 0–400 b/s | / | Not needed | 10 kHz | Low | 1.5 ON-OFF/Period | Needed | 2.5 ms |
| [24] | VZVWM | SVPWM | 0–50 b/s | Low | Not needed | 20 kHz | Low | 1 ON-OFF/Period | Not needed | 20 ms |
| This work | VZVPM | SVPWM | 0–100 b/s | Low | Not needed | 10 kHz | Low | 1 ON-OFF/Period | Not needed | 12.5 ms |

For three-phase dc–ac TPC, most of them modulate the data by changing the carrier frequency or superimposing frequency-hopping sinusoidal carriers based on sinusoidal pulse width modulation (SPWM) control [15], [16]. In [17], modulated by RS-TPC-ASK (ON–OFF keying), the fractional harmonic current space vector is superimposed on the current reference in the internal current loops of the converter on the $dq$ frame to achieve dc–ac TPC. In [18], binary PSK modulated CS-TPC is introduced into an SPWM-controlled dc–ac converter, and data are demodulated from the phase of side-band harmonics. However, FSK methods could degrade power quality and stability from a power system perspective. Phase-shifting the carrier introduces additional switching operations that increase power losses and voltage fluctuations. In smart grids, bit rate and latency are important communication metrics because high bit rate and low latency can extend the reach of the application, and low latency can prevent instability [19]. Data volume of secondary control is less than 100 B, and stability can be achieved by carefully selecting the maximum communication delay, which depends heavily on the control parameters [20]. A review on maximum latency for secondary control in islanded microgrids is given in [21], and it varies from 0.06 to 10 s. Tertiary control is typically implemented for energy management systems and other monitoring/metering purposes, where low-priority data packets are delivered at a low sampling rate (several seconds or minutes). DC–DC TPC has a maximum bit rate of up to Mb/s, and dc–ac TPC has a maximum bit rate of hundreds of b/s with a latency of less than 20 ms [15]. TPC could, therefore, be applied to smart grids for secondary and tertiary control.

For three-phase dc–ac inverters, due to the high dc-link voltage utilization, space vector pulsewidth modulation (SVPWM) has been widely used for decades, such as for renewable energy integration and motor drive system regulation [22]. It is interesting to note that SVPWM zero vectors, which have been applied to power conversion, offer some flexibility in concurrently embedding data to produce a new dc–ac TPC type. The idea of SVPWM-based three-phase dc–ac TPC technologies has been presented in [23], where the side-band harmonics were initially employed for TPC. However, theoretical foundations, the demodulation process, and communication effectiveness have not yet been determined. A variable zero-vector-width-based modulation (VZVWM) for three-phase dc–ac TPC has been comprehensively investigated in [24]. However, the achieved bit rate of VZVWM is poor due to the small resolution frequency required in the fast fourier transform (FFT) analysis.

This work aims to propose a new three-phase dc–ac TPC method based on the position of zero vectors varying. The harmonic distribution model is derived to provide a clear illustration of the demodulation process. Furthermore, the TPC optimization can be supported by the harmonic distribution model. This article takes into account the requirements for power quality and communication performance, and provides an alternative for communication in smart grids. A comparison between the proposed variable zero vector position modulation (VZVPM) technique and state-of-the-art three-phase dc–ac TPC approaches is summarized in Table I. The unique innovations and advances of the proposed VZVPM technique include the following.

1) Unlike FSK-based TPC, VZVPM does not require frequency hopping and can maintain a reduced $\Delta$ THD.
2) Unlike RS-TPC, VZVPM is independent of closed-loop and phase-locked loop control, avoiding instability crises and tricky controller design.
3) VZVPM does not split pulses and subsequently produce narrow pulse issues as CS-TPC-PSK does. Furthermore, no extra switching losses are required.
4) Compared to existing zero vector modulation (VZVWM), VZVPM doubles the bit rate with half the switching frequency and half the number of FFT points.

The main contributions of this article are as follows.

1) A novel VZVPM and its corresponding demodulation method are proposed.
2) An analysis is conducted on the harmonic characteristic model of variable zero vector position-based modulation, which provides mathematical support for bit-rate optimization and sliding FFT-based demodulation.
3) Bit error rates at various line distances and zero-vector positions are shown, which is rarely discussed

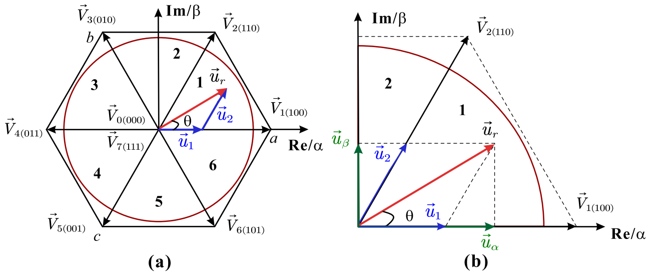

Fig. 1. Illustration of SVPWM. (a) Space vectors. (b) Modulation.

for TPC in the literature, demonstrating the usefulness for harsh environments, i.e., for channels with low SNR.

4) Hardware experiments validate the feasibility of our proposed VZVPM technique and the ability to transmit data across the transformer.

The rest of this article is organized as follows. Section II introduces the principle of VZVPM and an application scenario of VZVPM-based TPC for microgrid condition monitoring. In Section III, a mathematical model of harmonic distribution for VZVPM-based TPC is built, and harmonic characteristic-based demodulation for VZVPM-based TPC is elaborated. In Section IV, the feasibility of the proposed VZVPM-based dc–ac TPC technique has been validated, and the communication performance is demonstrated through simulations and experiments. Finally, Section V concludes this article.

## II. PRINCIPLE OF VARIABLE ZERO VECTOR POSITION TALKATIVE MODULATION

### A. *Basics of SVPWM in DC–AC Talkative Converters*

An illustration of SVPWM for two-level converters is shown in Fig. 1. The space vector trajectory is located inside a hexagon, which is composed of six active vectors and two zero vectors. The hexagon is divided into six sectors (i.e., sector-1,..., sector-6). Taking the reference vector $\vec{u}_r$ in sector-1 as an example, the output vector $\vec{u}_r$ can be expressed by

$$\vec{u}_r = \vec{u}_1 + \vec{u}_2 = \frac{T_1}{T_\mathrm{s}}\vec{V}_1 + \frac{T_2}{T_\mathrm{s}}\vec{V}_2 \tag{1}$$

where $T_\mathrm{s}$ is the switching period, $T_1$ and $T_2$ are the active times of $\vec{V}_1$ and $\vec{V}_2$, which are the neighboring space vectors of $\vec{u}_r$ in a switching period, respectively.

Based on Fig. 1(b), and the volt-second equilibrium principle, it can be deduced that

$$\begin{cases} T_1 = \frac{\sqrt{3}T_\mathrm{s}}{2U_\mathrm{dc}}\left(\sqrt{3}u_\alpha - u_\beta\right) \\ T_2 = \frac{\sqrt{3}T_\mathrm{s}}{E}u_\beta \end{cases} \tag{2}$$

where $U_\mathrm{dc}$ is the dc-link voltage, and $u_\alpha$ and $u_\beta$ are real and imaginary parts of $\vec{u}_r$, respectively. In a switching period

$$T_1 + T_2 + T_0 = T_\mathrm{s} \tag{3}$$

where $T_0$ is the sum of active time intervals of zero vectors $\vec{V}_0$ and $\vec{V}_7$. Power conversion determines the active times of the zero vectors and other space vectors. However, in a switching cycle, there are different degrees of freedom in the distribution of space vector sequence. Although the action time of the space vectors is fixed, the position of the zero vectors can be changed independently. This feature enables TPC by integrating the information into the position of the zero vectors.

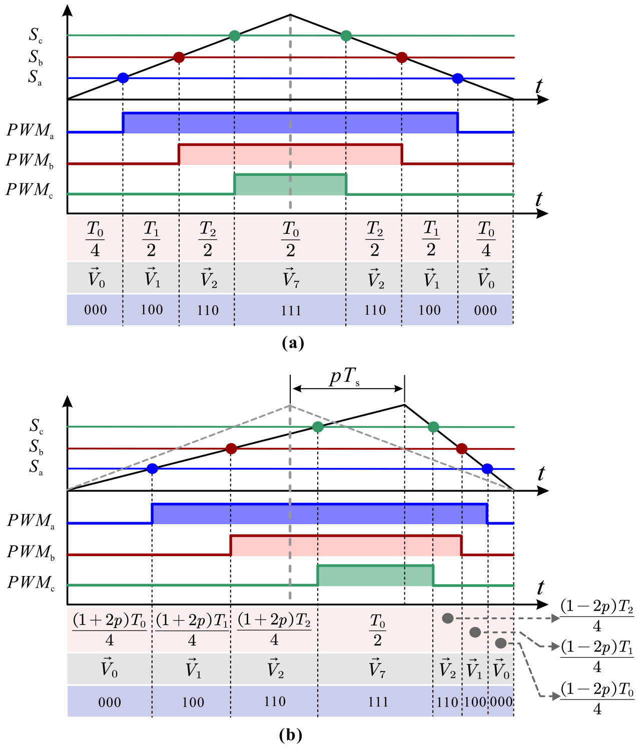

Fig. 2. Sector 1 for VZVPM-based TPC. (a) For bit “1”. (b) For bit “0”.

### B. *VZVPM*

In the proposed version of VZVPM, the action positions of the zero vectors are shifted. Taking the 7-segment SVPWM as an example, the VZVPM in sector 1 for TPC is depicted in Fig. 2. A simple way to implement it is by shifting the peak position of the triangular carrier. The isosceles triangular carrier is used to transmit bit “1,” while bit “0” transmission requires triangular carriers with the peak position shifted to the left or right. Assuming that the distance between the peak position of the carrier for bit “0” and that for “1” equals $pT_s$ ($p \neq 0$), then $p$ is positive with peak position shifted rightward and negative for leftward-shifted position. Hence, $p$ ranges from $-0.5$ to 0.5, and the triangular carrier becomes a sawtooth wave at $p = \pm 0.5$.

From a power perspective, VZVPM is superior to FSK because of its constant switching frequency. VZVPM also has advantages over PSK. The gate drive comparison of PSK and the proposed VZVPM technique is shown in Fig. 3. First, assuming that bits “0” and “1” occur evenly in a bit sequence, PSK turns ON and OFF 1.5 times per period, while VZVPM turns ON and OFF once per period. This indicates that VZVPM requires no additional switching power loss, while PSK requires 0.5 times more switching than VZVPM. Second, when the carrier phase is

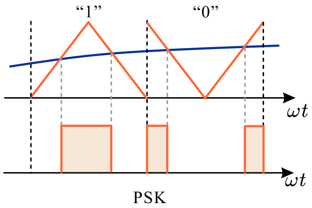

Fig. 3. Gate drive comparison of PSK and VZVPM.

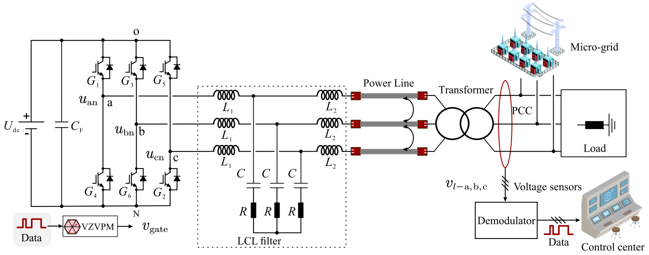

Fig. 4. VZVPM for three-phase DC–AC TPC.

180°, one pulse in PSK is split into two pulses in one switching period, while only one pulse is generated in one switching period in VZVPM. PSK pulse splitting can result in a narrower pulse width. In fact, narrow pulses are more likely to be distorted and lost, and this problem becomes much worse with small duty cycles.

VZVPM for three-phase dc–ac TPC is demonstrated in Fig. 4. Data are mapped to gate drive positions based on VZVPM. The data-carrying power then travels through an $LCL$ filter and the power line to the point of common coupling (PCC), where the load and other branches of the microgrid are connected. By sampling and analyzing voltages at the PCC, a nearby control center collect data to improve their decision-making processes.

## III. HARMONIC CHARACTERISTICS-BASED DEMODULATION FOR VZVPM-BASED TPC

### A. *Harmonic Characteristics Analysis*

VZVPM-based TPC generates a time-varying harmonic distribution of the output voltages in which the data is embedded. Since the output voltages are generated by comparing the references $S_{a,b,c}$ with the carrier, both the frequency of the references and the switching frequency are introduced. The time-varying switched waveform can be expressed in sinusoidal harmonic components as

$$F\left(\omega_s t, \omega_o t\right) = \sum_{m=0}^{m=\infty} \sum_{n=-\infty}^{n=\infty} C_{mn} \mathrm{e}^{\mathrm{j}(m\omega_s t + n\omega_o t)}. \tag{4}$$

It includes the dc offset, fundamental and baseband harmonics, carrier harmonics, and carrier sideband harmonics. The harmonic coefficients can be calculated by

$$C_{mn} = A_{mn} + \mathrm{j}B_{mn} = \frac{1}{2\pi^2} \int_{-\pi}^{\pi} \int_{-\pi}^{\pi} F(x,y) \mathrm{e}^{\mathrm{j}(mx+ny)} dxdy \tag{5}$$

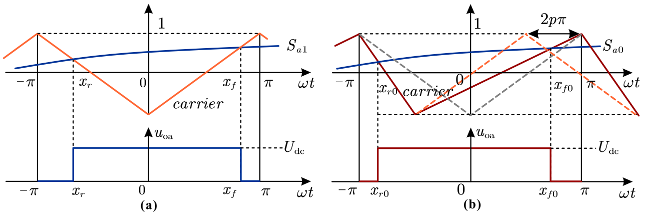

Fig. 5. Inner integral limits of VZVPM for naturally sampled PWM. (a) for bit "1." (b) for bit "0."

where $x = \omega_s t$, $y = \omega_o t$, and $\omega_s$ and $\omega_o$ are the switching frequency and fundamental frequency, respectively.

Fig. 5(a) illustrates naturally sampled PWM. In a three-phase two-level voltage source inverter, the voltage on the phase-a upper switch $u_{oa}$ is equal to $U_{dc}$ within two points of intersection $x_r$ and $x_f$, which creates the inner integral limits in harmonic coefficients calculation, viz

$$C_{mn} = \frac{U_{dc}}{2\pi^2} \int_{-\pi}^{\pi} \int_{x_r}^{x_f} \mathrm{e}^{\mathrm{j}(mx+ny)} dxdy. \tag{6}$$

Taking the voltages on upper switches of phase-a and -b $(u_{oa}, u_{ob})$ as an example, they can be expressed by double Fourier series as

$$\begin{cases} u_{oa}(x,y) = \sum_{m=0}^{m=\infty} \sum_{n=-\infty}^{n=\infty} C_{mn} \mathrm{e}^{\mathrm{j}(mx+ny)} \\ u_{ob}(x,y) = \sum_{m=0}^{m=\infty} \sum_{n=-\infty}^{n=\infty} C_{mn} \mathrm{e}^{\mathrm{j}(mx+n(y-2\pi/3))}. \end{cases} \tag{7}$$

Hence, the line-to-line voltage $u_{ab}$ can be written as

$$u_{ab}(x,y) = \sum_{m=0}^{m=\infty} \sum_{n=-\infty}^{n=\infty} \lambda_n C_{mn} \mathrm{e}^{\mathrm{j}(mx+ny)} \tag{8}$$

where $\lambda_n = \mathrm{e}^{-\mathrm{j}\frac{2n\pi}{3}} - 1$. For line-to-line voltages, there is no harmonic component at the switching frequency since $n = 0$, resulting in $\lambda_n = 0$.

*1) Harmonic Distributions of VZVPM-Based TPC for Sending Bit "1":* Function of $S_{a1}(y,i)$ can be expressed by

$$S_{a1}(y,i) = \begin{cases} \frac{\sqrt{3}}{2} M \cos\left(y - \frac{\pi}{6}\right), y \in \left[0, \frac{\pi}{3}\right) \cup \left[-\pi, -\frac{2\pi}{3}\right), i = 3,6 \\ \frac{3}{2} M \cos y, \quad y \in \left[\frac{\pi}{3}, \frac{2\pi}{3}\right) \cup \left[-\frac{2\pi}{3}, -\frac{\pi}{3}\right), i = 2,5 \\ \frac{\sqrt{3}}{2} M \cos\left(y + \frac{\pi}{6}\right), y \in \left[\frac{2\pi}{3}, \pi\right) \cup \left[-\frac{\pi}{3}, 0\right), i = 1,4 \end{cases} \tag{9}$$

where $M = 2|u_a|/U_{dc}$, $u_a$ is the phase voltage, and $i$ is the sector index from 1 to 6.

For SVPWM, references include six segments. The general harmonic coefficients can be calculated by

$$C_{mn-1} = \frac{U_{dc}}{2\pi^2} \sum_{i=1}^{6} \int_{y_s(i)}^{y_e(i)} \int_{x_r(i)}^{x_f(i)} \mathrm{e}^{\mathrm{j}(mx+ny)} dxdy. \tag{10}$$

The outer and inner integral limits for centered SVPWM reference waveforms are given in Table I.

*2) Harmonic Distributions of VZVPM-Based TPC for Sending Bit "0":* The inner integral limits of VZVPM when sending bit “0” are shown in Fig. 5(b), and the reference $S_{a0}(y,i)$ equals $S_{a1}(y,i)$. The inner integral limits can be deduced as

$$\begin{aligned} x_{r0}(i) &= -\frac{(1-2p)\pi}{2}\left(S_{a0}(y)+\frac{1+2p}{1-2p}\right) \\ &= (1-2p)x_r(i) - 2p\pi \\ x_{f0}(i) &= \frac{(1+2p)\pi}{2}\left(S_{a0}(y)+\frac{1-2p}{1+2p}\right) \\ &= (1+2p)x_f(i) - 2p\pi. \end{aligned} \tag{11}$$

Particularly, the carrier evolves to the sawtooth wave when $p = \pm 0.5$. If $p = 0.5$, $x_{r0}(i) = -\pi$, and $x_{f0}(i) = \pi S_{a0}(y,i)$; if $p = -0.5$, $x_{r0}(i) = -\pi S_{a0}(y,i)$, and $x_{f0}(i) = \pi$. Hence, the harmonic coefficients $C_{mn-0}$ for bit “0” becomes

$$C_{mn-0} = \frac{U_{\mathrm{dc}}}{2\pi^2}\sum_{i=1}^{6}\int_{y_s(i)}^{y_e(i)}\int_{x_{r0}(i)}^{x_{f0}(i)} \mathrm{e}^{\mathrm{j}(mx+ny)}\,dx\,dy. \tag{12}$$

For $m = n = 0$, because $x_f(i) + x_r(i) = 0$, $C_{00-0} = C_{00-1} = U_{\mathrm{dc}}$. For $m = 0, n > 0$, $C_{0n-0} = C_{0n-1}$. For $m > 0$, it can be deduced that

$$\begin{aligned} C_{mn-0} &= \frac{U_{\mathrm{dc}}}{2\mathrm{j}m\pi^2}\mathrm{e}^{-2\mathrm{j}mp\pi} \\ &\times \sum_{i=1}^{6}\int_{y_s(i)}^{y_e(i)} \mathrm{e}^{\mathrm{j}ny}\begin{bmatrix} \mathrm{e}^{\mathrm{j}\frac{m\pi(1+2p)}{2}}\mathrm{e}^{\mathrm{j}\frac{(1+2p)\pi m S_{a1}(y,i)}{2}} \\ -\mathrm{e}^{-\mathrm{j}\frac{m\pi(1-2p)}{2}}\mathrm{e}^{-\mathrm{j}\frac{(1-2p)\pi m S_{a1}(y,i)}{2}} \end{bmatrix} dy. \end{aligned} \tag{13}$$

Based on the complex form of the Jacobi–Anger expansions [25, Appendix 2], (13) can be simplified as

$$C_{mn-0} = \frac{U_{\mathrm{dc}}}{2\mathrm{j}\mathrm{m}\pi^2}\sum_{i=1}^{6}\int_{y_s(i)}^{y_e(i)} \Pi_i\, dy \tag{14}$$

where

$$\begin{aligned} \Pi_i &= \mathrm{e}^{\mathrm{j}ny} \\ &\times \begin{bmatrix} \mathrm{e}^{\mathrm{j}\frac{\mathrm{m}\pi(1-2\mathrm{p})}{2}}\mathrm{J}_0\left(\alpha_{\mathrm{i}+}\right) - \mathrm{e}^{-\mathrm{j}\frac{\mathrm{m}\pi(1+2\mathrm{p})}{2}}\mathrm{J}_0\left(\alpha_{\mathrm{i}-}\right) \\ +2\sum_{k=1}^{\infty}\cos\left(k[y+\beta_i]\right) \\ \times\left[\mathrm{e}^{\mathrm{j}\frac{\pi[m(1-2p)+k]}{2}}J_k\left(\alpha_{i+}\right) - \mathrm{e}^{-\mathrm{j}\frac{\pi[m(1+2p)+k]}{2}}J_k\left(\alpha_{i-}\right)\right] \end{bmatrix} \end{aligned} \tag{15}$$

where $\alpha_{1,3,4,6+} = \frac{\sqrt{3}(1+2p)\pi m M}{4}$, $\alpha_{1,3,4,6-} = \frac{\sqrt{3}(1-2p)\pi m M}{4}$, $\alpha_{2,5+} = \frac{3(1+2p)\pi m M}{4}$, $\alpha_{2,5-} = \frac{3(1-2p)\pi m M}{4}$, $\beta_{1,4} = \frac{\pi}{6}$, $\beta_{2,5} = 0$, and $\beta_{3,6} = -\frac{\pi}{6}$. Then, (14) can be integrated to

$$C_{mn-0} = \frac{U_{\mathrm{dc}}}{2m\pi^2}\begin{bmatrix} \Lambda_1\left.\right|_{\frac{2\pi}{3}}^{\pi} + \Lambda_2\left.\right|_{\frac{\pi}{3}}^{\frac{2\pi}{3}} + \Lambda_3\left.\right|_{0}^{\frac{\pi}{3}} \\ +\Lambda_4\left.\right|_{-\frac{\pi}{3}}^{0} + \Lambda_5\left.\right|_{-\frac{2\pi}{3}}^{-\frac{\pi}{3}} + \Lambda_6\left.\right|_{-\pi}^{-\frac{2\pi}{3}} \end{bmatrix} \tag{16}$$

where

$$\begin{aligned} &\Lambda_i \\ &= \begin{bmatrix} \xi_0(\alpha_i)\frac{\mathrm{e}^{\mathrm{j}ny}}{\mathrm{j}n} + \xi_n(\alpha_i)\mathrm{e}^{-\mathrm{j}n\beta_i}y\left.\right|_{k=|n|} + \sum_{k=1}^{\infty}\xi_k(\alpha_i) \\ \times\left[\frac{\mathrm{e}^{\mathrm{j}\left([n+k]y+k\beta_i\right)}}{j[n+k]}\left.\right|_{k\neq -n} + \frac{\mathrm{e}^{\mathrm{j}\left([n-k]y-k\beta_i\right)}}{\mathrm{j}[n-k]}\left.\right|_{k\neq n}\right] \end{bmatrix} \end{aligned} \tag{17}$$

given the definitions, (18) shown at the bottom of the next page.

With considerable manipulation, the harmonic coefficients or coefficient $C_{mn-0}$ can be deduced, as shown in (19). Note that this solution is also valid when $m > 0, n = 0$, and (19), shown at the bottom of the next page, coincides with the harmonic results of the centered SVPWM when $p = 0$ [25, Ch. 6]. Due to the movement of the peak position, as shown in (18), Bessel function parts along with their exponential coefficients become asymmetric, reshaping the amplitude and phase of the harmonics. Therefore, by searching for harmonic coefficients with large disparities for bits “1” and “0,” data can be demodulated from the magnitude or phase of these targeted harmonics.

The presence of both relatively high-amplitude and high-frequency data-carrying harmonics is critical because weak harmonics are difficult to detect at the demodulator end, and low-frequency harmonics limit the bit rate. The harmonics, which are close to integer multiples of the switching frequency, have greater amplitude and higher frequency, making them suitable as data carriers in TPC. Therefore, the harmonic coefficients in the vicinity of the switching frequency should be the main focus of the TPC based on the harmonic characteristic. At switching frequency, there is $m = 1$ in (19), and the definitions in (18) are simplified as

$$\begin{cases} \xi_0(\alpha_i) = \mathrm{e}^{-\mathrm{j}\pi p}J_0(\alpha_{i+}) + \mathrm{e}^{\mathrm{j}\pi p}J_0(\alpha_{i-}) \\ \xi_n(\alpha_i) = \mathrm{e}^{-\mathrm{j}\pi(p-\frac{n}{2})}J_n(\alpha_{i+}) + \mathrm{e}^{\mathrm{j}\pi(p-\frac{n}{2})}J_n(\alpha_{i-}) \\ \xi_k(\alpha_i) = \mathrm{e}^{-\mathrm{j}\pi(p-\frac{k}{2})}J_k(\alpha_{i+}) + \mathrm{e}^{\mathrm{j}\pi(p-\frac{n}{2})}J_k(\alpha_{i-}). \end{cases} \tag{20}$$

It can be seen that in (19), except for $\xi_{0,n,k}(\alpha_i)$, no component is related to position $p$. Hence, the value of $C_{mn-0}$ is changed by $\xi_{0,n,k}(\alpha_i)$ when the position shifts. The expression $\xi_{0,n,k}(\alpha_i)$ is symmetric with respect to $p = 0$, which means that the value of $C_{mn-0}$ is also symmetric about $p = 0$. Taking $\xi_0(\alpha_i)$ as an example, the magnitude difference of $\xi_0(\alpha_i)$ for bit “0” and “1” is

$$\Delta\xi_0(\alpha_i) = \mathrm{e}^{-\mathrm{j}\pi p}J_0(\alpha_{i+}) + \mathrm{e}^{\mathrm{j}\pi p}J_0(\alpha_{i-}) - 2J_0(\alpha_i) \tag{21}$$

where $\alpha_i = \alpha_{i+} = \alpha_{i-}$ when $p = 0$. Similarly, $\xi_n(\alpha_i)$ and $\xi_k(\alpha_i)$ have the same properties. Then, a rough and accessible magnitude analysis could be done from $\xi_0(\alpha_i)$ and $\Delta\xi_0(\alpha_i)$.

To verify this derivation, based on (8) and (19) and taking $M$=0.7333 as an example, the theoretical harmonic amplitudes of $u_{\mathrm{oa}}$ and $u_{\mathrm{ab}}$ over the dc-link voltage $U_{\mathrm{dc}}$ at some target harmonics $\omega_{\mathrm{s}} \pm n\omega_{\mathrm{o}}$ with different $p$ are drawn in Fig. 6. The harmonics are distributed symmetrically around $p = 0$, with the harmonic amplitude of $u_{\mathrm{oa}}$ bulging at $\omega_{\mathrm{s}}$ $(n = 0)$, while the amplitudes of other sideband harmonics of both $u_{\mathrm{oa}}$ and $u_{\mathrm{ab}}$ decrease nonlinearly to different extents as $p$ moves from $\pm 0.5$ to 0. Theoretically, the target harmonics for demodulation can be any harmonic that changes with the variation of $p$.

*3) Influence of Dead Time on Harmonic Analysis:* Dead time is necessary in experiments to avoid a short circuit that occurs when the top and bottom switches of one leg are operated simultaneously. Since the dead time in the experiment would slightly affect the harmonic characteristics, a harmonic characteristic should be analyzed taking into account the dead time effect.

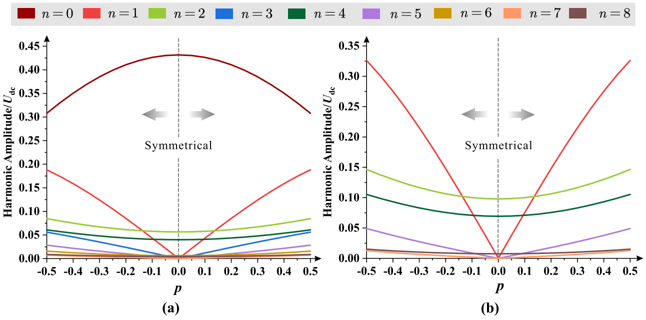

Fig. 6. Theoretical harmonic amplitudes of (a) $u_{\text{oa}}$ and (b) $u_{\text{ab}}$ over the dc-link voltage at harmonics $\omega_{\text{s}} \pm n\omega_{\text{o}}$ with different $p$.

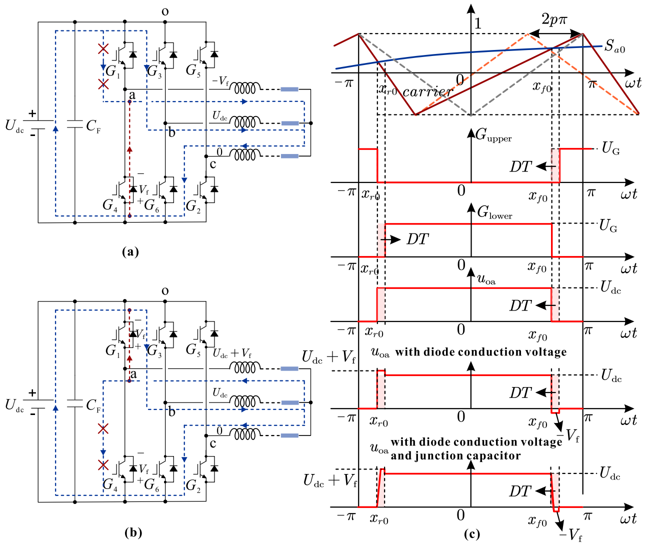

Fig. 7. Inner integral limits of VZVPM for naturally sampled PWM with dead time. (a) Current flow in dead time before $x_{r0}$. (b) Current flow in dead time after $x_{f0}$. (c) Waveforms of drive pulse and $u_{\text{oa}}$.

Assuming that the dead time on the rising and falling edges of the pulse is the same and equal to $2\pi \text{DT} f_{\text{s}}$, the interintegral limits of VZVPM for linearly sampled PWM taking dead time into account are shown in Fig. 7. Taking sector 2 as an example, Fig. 7(a) and (b) shows the current flow in the dead time before $x_{r0}$ and after $x_{f0}$, and the voltages at node-a,b,c are marked. If both the upper and lower switches in leg-a are OFF in the dead time, the inductor current in phase-a would flow through the freewheeling diodes of the switch where current flowed through its complementary switch before the dead time. Ignoring the diode conduction voltage $V_{\text{f}}$ and the transient switching process, the inner integral limits of $u_{\text{oa}}$ are the same as those without dead time, meaning that the dead time has little effect on the harmonic characteristics. Considering the diode conduction voltage, the value of $u_{\text{oa}}$ is $U_{\text{dc}} + V_{\text{f}}$ during the dead time before $x_{r0}$ and $-V_{\text{f}}$ during the dead time after $x_{f0}$. Then, according to (12), the difference of the coefficients for $u_{\text{oa}}$ is

$$\begin{aligned} &C_{mn-\text{DT}} - C_{mn0} \\ &\quad = \frac{V_{\text{f}}}{2\pi^2} \sum_{i=1}^{6} \int_{y_s(i)}^{y_e(i)} \int_{x_{r0}(i)}^{x_{r0}(i)+\text{DT}} \mathrm{e}^{\mathrm{j}(mx+ny)} dxdy \\ &\quad\quad - \frac{V_{\text{f}}}{2\pi^2} \sum_{i=1}^{6} \int_{y_s(i)}^{y_e(i)} \int_{x_{f0}(i)}^{x_{f0}(i)+\text{DT}} \mathrm{e}^{\mathrm{j}(mx+ny)} dxdy \end{aligned} \tag{22}$$

where $C_{mn-\text{DT}}$ and $C_{mn0}$ are the harmonic coefficients with and without dead time, respectively. Since $V_f$ is small compared to $U_{\text{dc}}$, this coefficient difference is trivial.

In practice, there is transient behavior during the dead time due to the junction capacitor in the switch, and the rising and falling edges are not ideally vertical. In this case, according to the volt-second balance rule, the integration of $u_{\text{oa}}$ in the dead time can correspond to a rectangle with a constant height $U_{\text{dc}}$ and a duration ($\text{DT}_1'$ or $\text{DT}_2'$), namely

$$\begin{cases} \int_{x_{r0}(i)}^{x_{r0}(i)+\text{DT}} u_{\text{oa}}(\omega t) d\omega t = U_{\text{dc}} \text{DT}_1' \\ \int_{x_{f0}(i)}^{x_{f0}(i)+\text{DT}} u_{\text{oa}}(\omega t) d\omega t = U_{\text{dc}} \text{DT}_2'. \end{cases} \tag{23}$$

Then, the inner integral limits of the coefficients can be updated as $x_{r0}(i) + \text{DT} - \text{DT}_1'$ and $x_{f0}(i) + \text{DT}_2'$, and the universal harmonic coefficient becomes

$$C_{mn-\text{DT}} = \frac{U_{\text{dc}}}{2\pi^2} \sum_{i=1}^{6} \int_{y_s(i)}^{y_e(i)} \int_{x_{r0}(i)+\text{DT}-\text{DT}_1'}^{x_{f0}(i)+\text{DT}_2'} \mathrm{e}^{\mathrm{j}(mx+ny)} dxdy. \tag{24}$$

However, the analysis is complicated because the waveform of $u_{\text{oa}}$ in the dead time depends on the load, diode conduction voltage, switch parasitics and $LCL$ filter inductance. Simulations could be more realistic to analyze the harmonic when the dead time is long and the parasitic parameters have a significant effect.

### B. *Demodulation of VZVPM-Based DC–AC TPC*

*1) Demodulation Process:* As analyzed above, the data are embedded in the variation of $p$, resulting in a nonlinear amplitude divergence at some target harmonics. Aiming to that,

$$\begin{cases} \xi_0(\alpha_i) = \mathrm{e}^{\frac{-\mathrm{j}\pi[1-m(1-2p)]}{2}} J_0(\alpha_{i+}) + \mathrm{e}^{\frac{\mathrm{j}\pi[1-m(1+2p)]}{2}} J_0(\alpha_{i-}) \\ \xi_n(\alpha_i) = \mathrm{e}^{\frac{-\mathrm{j}\pi[1-m(1-2p)-n]}{2}} J_n(\alpha_{i+}) + \mathrm{e}^{\frac{\mathrm{j}\pi[1-m(1+2p)-n]}{2}} J_n(\alpha_{i-}) \\ \xi_k(\alpha_i) = \mathrm{e}^{\frac{-\mathrm{j}\pi[1-m(1-2p)-k]}{2}} J_k(\alpha_{i+}) + \mathrm{e}^{\frac{\mathrm{j}\pi[1-m(1+2p)-k]}{2}} J_k(\alpha_{i-}) \end{cases} \tag{18}$$

$$C_{mn-0} = \frac{2U_{\text{dc}}}{m\pi^2} \left[ \begin{array}{c} \frac{\pi}{6}\left[2\cos\frac{n\pi}{6}\xi_n(\alpha_1) + \xi_n(\alpha_2)\right] + \frac{1}{n}\sin\frac{n\pi}{6}\cos\frac{n\pi}{2}\left[\xi_0(\alpha_2) - \xi_0(\alpha_1)\right]|_{n\neq 0} \\ +\sum_{k=1,k\neq -n}^{\infty}\left[\frac{1}{[n+k]}\sin\frac{[n+k]\pi}{6}\cos\frac{[n+k]\pi}{2}\left\{2\cos\frac{[2n+3k]\pi}{6}\xi_k(\alpha_1) + \xi_k(\alpha_2)\right\}\right] \\ +\sum_{k=1,k\neq n}^{\infty}\left[\frac{1}{[n-k]}\sin\frac{[n-k]\pi}{6}\cos\frac{[n-k]\pi}{2}\left\{2\cos\frac{[2n-3k]\pi}{3}\xi_k(\alpha_1) + \xi_k(\alpha_2)\right\}\right] \end{array} \right]. \tag{19}$$

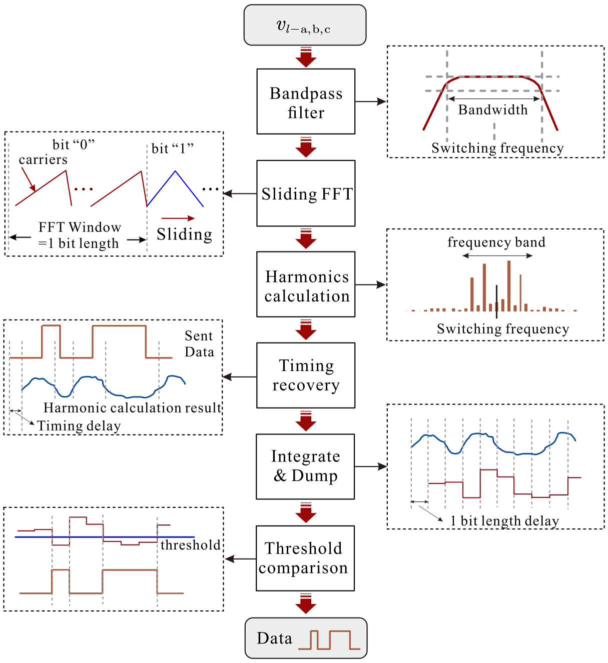

Fig. 8. Demodulation schematic based on sliding FFT.

TABLE II
OUTER AND INNER INTEGRAL LIMITS FOR CENTERED SVPWM REFERENCE WAVEFORMS [25, CH. 6]

| $i$ | $y_s(i)$ | $y_e(i)$ | $x_r(i)$ | $x_f(i)$ |
|---|---|---|---|---|
| 1 | $\frac{2\pi}{3}$ | $\pi$ | $-\frac{\pi}{2}[1+\frac{\sqrt{3}}{2}M\cos(y+\frac{\pi}{6})]$ | $\frac{\pi}{2}[1+\frac{\sqrt{3}}{2}M\cos(y+\frac{\pi}{6})]$ |
| 2 | $\frac{\pi}{3}$ | $\frac{2\pi}{3}$ | $-\frac{\pi}{2}[1+\frac{3}{2}M\cos(y)]$ | $\frac{\pi}{2}[1+\frac{3}{2}M\cos(y)]$ |
| 3 | 0 | $\frac{\pi}{3}$ | $-\frac{\pi}{2}[1+\frac{\sqrt{3}}{2}M\cos(y-\frac{\pi}{6})]$ | $\frac{\pi}{2}[1+\frac{\sqrt{3}}{2}M\cos(y-\frac{\pi}{6})]$ |
| 4 | $-\frac{\pi}{3}$ | 0 | $-\frac{\pi}{2}[1+\frac{\sqrt{3}}{2}M\cos(y+\frac{\pi}{6})]$ | $\frac{\pi}{2}[1+\frac{\sqrt{3}}{2}M\cos(y+\frac{\pi}{6})]$ |
| 5 | $-\frac{2\pi}{3}$ | $-\frac{\pi}{3}$ | $-\frac{\pi}{2}[1+\frac{3}{2}M\cos(y)]$ | $\frac{\pi}{2}[1+\frac{3}{2}M\cos(y)]$ |
| 6 | $-\pi$ | $-\frac{2\pi}{3}$ | $-\frac{\pi}{2}[1+\frac{\sqrt{3}}{2}M\cos(y-\frac{\pi}{6})]$ | $\frac{\pi}{2}[1+\frac{\sqrt{3}}{2}M\cos(y-\frac{\pi}{6})]$ |

TABLE III
LIST OF SYSTEM PARAMETERS

| **Variables** | **Symbols** | **Values** |
|---|---|---|
| Damping resistance of $LCL$ filter ($\Omega$) | $R$ | 1 |
| Inductances of $LCL$ filter (mH) | $L_{1,2}$ | 2 |
| DC-link capacitance (mF) | $C_\mathrm{F}$ | 4 |
| Capacitance of $LCL$ filter ($\mu$F) | $C$ | 10 |
| DC-link voltage (V) | $U_\mathrm{dc}$ | 600 |
| Load (kW) | $Z$ | $3\phi$, 8 |
| Switching frequency (kHz) | $f_\mathrm{s}$ ($\omega_\mathrm{s}/2\pi$) | 10 |
| Fundamental frequency (Hz) | $f_\mathrm{o}$ ($\omega_\mathrm{o}/2\pi$) | 50 |
| Amplitude of line-to-line voltage (V) | $\lvert u_\mathrm{ab}\rvert$ | 380 |
| Sampling frequency (kHz) | $F$ | 100 |
| FFT points in the sliding window | $N$ | 500 |
| Positive-sequence resistance ($\Omega$) | $r_1$ | 0.871 |
| Positive-sequence inductance (mH) | $l_1$ | 1.62 |
| Zero-sequence resistance ($\Omega$) | $r_0$ | 3.48 |
| Zero-sequence inductance (mH) | $l_0$ | 8.18 |

the sliding-FFT-based demodulation algorithm is proposed as shown in Fig. 8. A bandpass filter with the center frequency equal to the switching frequency is used to filter the PCC voltages $v_{l-\mathrm{a,b,c}}$. Then, the sliding FFT is used, with a window width equal to one bit length. Magnitudes of the target harmonics are calculated and updated online. As there is a time delay between the transmitted data and the result of the harmonic calculation, timing recovery is required to specify the start of the integration and dump process. An alternately hopped sequence of data is used to estimate the timing error. Theoretically, the harmonic result also rises and falls alternately. By comparing the peak timing of harmonic result with the transmitted data, the time delay can be estimated [24]. Ignoring the result of the harmonic calculation at the time delay slot, the output result is integrated into a sliding window of the same width as one bit length and then output online. The data can be demodulated by comparing the dumped value with the configured threshold, as the data are determined to be "0" if the dumped value is above the threshold and "1" otherwise.

*2) Bit Rate:* In a sliding FFT window

$$o/N = f/F \tag{25}$$

where $o$ is the harmonic order, $N$ is the number of points in a sliding window, $f$ is the target frequency to be observed, and $F$ is the sampling frequency. A larger $F$ and $N$ means an accurate FFT result and more reliable demodulation. The width of sliding FFT window equals one bit duration since it takes a window width to calculate the amplitude of targeted harmonics. Then, the bit rate $B$ is

$$B = F/N. \tag{26}$$

However, since both $o$ and $N$ are integers, the minimum order resolution $\Delta o = 1$ and the resolution frequency $\Delta f$, which represents the interval between two nearby harmonics on the spectrum, it follows

$$\Delta o/N = \Delta f/F \tag{27}$$

which indicates that a small resolution frequency $\Delta f$ during the harmonic computation limits the bit rate, and a wider FFT window is needed to draw the frequency spectrum with a smaller resolution frequency.

Consequently, the first upper limit of bit rate is from (25) and integer value of $o$. To increase the bit rate, target frequencies $f$ can be searched to make $F/N$ larger. The second limit on the bit rate is that the number of points $N$ in a sliding window cannot be too small. Otherwise, the FFT result will be inaccurate, resulting in a high bit error rate.

## IV. SIMULATIONS AND EXPERIMENTS VERIFICATION

A VZVPM-based dc–ac TPC system was simulated and experimentally verified, results are reported next.

### *A. Simulation Results*

Table III contains a list of system parameters [26]. The type of power line is chosen as SC-4×25 $\mathrm{mm}^2$ Cu. All capacitances

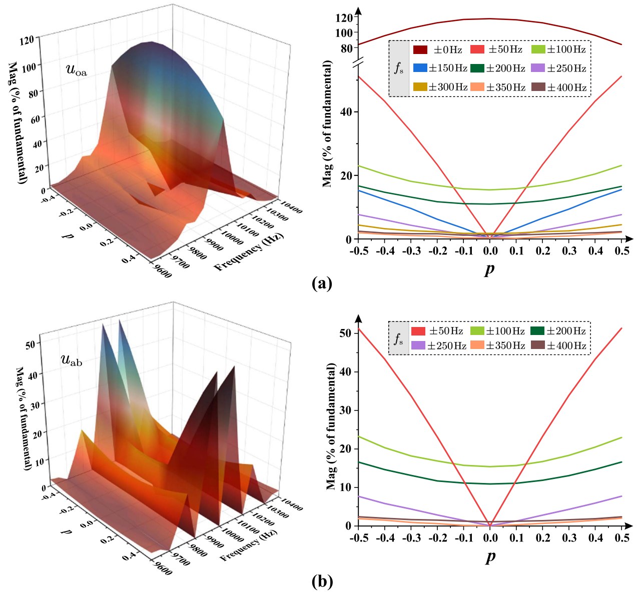

Fig. 9. Spectra of output voltages with variable zero vector positions. (a) $u_{\mathrm{oa}}$. (b) $u_{\mathrm{ab}}$.

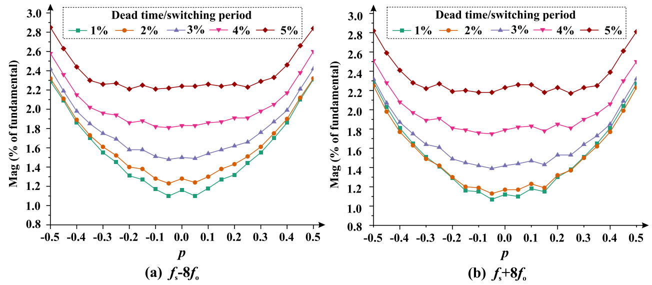

Fig. 10. Sideband harmonic magnitude of $u_{\mathrm{oa}}$ with different zero vector positions and dead times at (a) $f_{\mathrm{s}} - 8f_{\mathrm{o}}$ and (b) $f_{\mathrm{s}} + 8f_{\mathrm{o}}$.

to ground are ignored, and positive-sequence resistance and inductance are $r_1$, $l_1$, respectively, while zero-sequence resistance and inductance are $r_0$, $l_0$, respectively, all expressed in units of kilometers.

*1) Harmonics Distribution and THD Results:* Fig. 9(a) and (b) shows the spectra from 9.6 kHz to 10.4 kHz of $u_{\mathrm{oa}}$ and $u_{\mathrm{ab}}$ with varying zero vector positions, respectively. Both harmonics of $u_{\mathrm{oa}}$ and $u_{\mathrm{ab}}$ in simulation have the same pattern with the theoretical analysis as shown in Fig. 6. Taking the sideband harmonics at $f_{\mathrm{s}} \pm 8f_{\mathrm{o}}$ as an example, the sideband harmonic magnitude of $u_{\mathrm{oa}}$ at various positions and dead times is measured by simulation, as shown in Fig. 10. The ratio of dead time over switching period is changed from 1% to 5%. As the dead time increases, the magnitude of the sideband harmonics increases and becomes flat over a wider range of position $p$. The upper sideband frequency $f_{\mathrm{s}} + 8f_{\mathrm{o}}$ has a somewhat smaller magnitude than the lower sideband frequency $f_{\mathrm{s}} - 8f_{\mathrm{o}}$ due to dead time. By varying $p$, the magnitude of the sideband harmonics of $u_{\mathrm{oa}}$ jitters regionally, but is generally symmetrical about $p = 0$ and monotonous at both the left and right peak positions. The dead time has a negative effect on demodulation as the difference in magnitude for different bits becomes smaller, but the monotonicity of magnitude over position $p$ is evident with a dead time less than 3% of the switching period. Even with a dead time of 5% of the switching period, which is much longer than most cases, demodulation can still be robust by increasing the value of $p$ above 0.3.

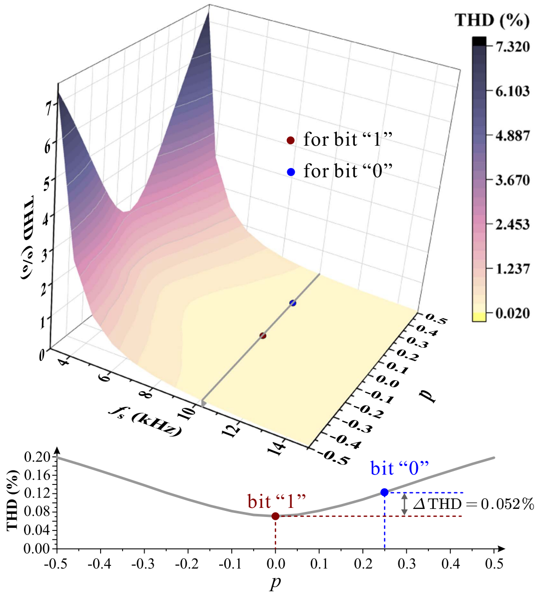

Fig. 11. THD results with diverse zero vector positions and switching frequencies.

THD results of sampled line-to-line voltages $v_{l-\mathrm{a,b,c}}$ with varying zero vector position $p$ and switching frequency $f_{\mathrm{s}}$ are shown in Fig. 11. The THD results meet the power quality requirements of the grid (THD<5%) over wide ranges of $f_{\mathrm{s}}$ and $p$, and decrease exponentially as $f_{\mathrm{s}}$ increases. The THD results are symmetric about and reach a minimum at $p$=0. When the $f_s$ is larger than 8 kHz, THD values are flat, i.e., robust to the variation of $p$. The operating points for bit "1" and "0" in the case study are marked in red and blue, respectively, and the THD results remain relatively low. The THD curve at 10 kHz is shown below in Fig. 11. The average THD at 10 kHz is 0.1295%, and the variation of THD is negligible (0.052%) as $p$ hops in communication.

*2) Modulation and Demodulation Results:* As a case study, bit "0" and "1" are mapped to $p = 0.25$ and $p = 0$, respectively. A 30 m long SC-4 × 25 mm$^2$Cu cable is used. Fig. 12 shows the waveforms of the transmitted data, output line-to-line voltage $u_{\mathrm{ab}}$, line currents $i_{\mathrm{a,b,c}}$, and line-to-line voltages $v_{l-\mathrm{a,b,c}}$ at the load side.

According to the harmonic distribution shown in Fig. 9(b), $f_{\mathrm{s}}$± 400 Hz can be selected as the targeted harmonic frequencies for both relatively higher bit rate and lower sampling frequency in practice. The result of the sliding FFT computation–$S_{\mathrm{FFT}}$, which is the sum of the harmonic percentages at $f_{\mathrm{s}}$± 400 Hz, is outputted after the noise outside of this frequency band is blocked by a bandpass Butterworth filter between 9.5 and 10.5 kHz. At a sampling rate of 100 kHz, 1k points in the

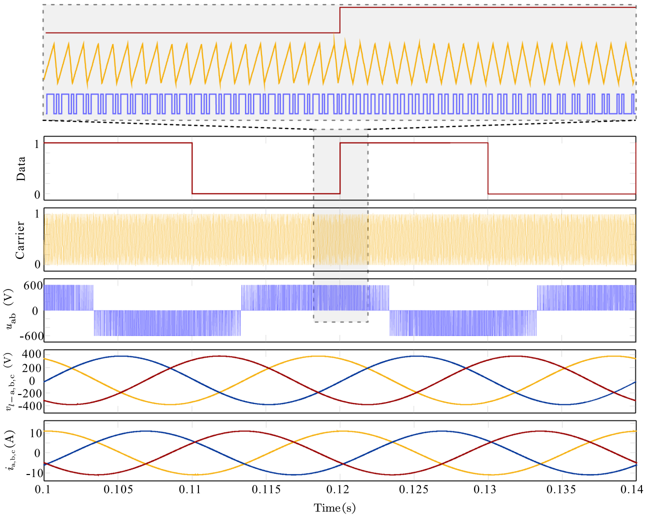

Fig. 12. Modulation waveforms of data, carrier, output voltage $u_{\text{ab}}$, line-to-line voltages $v_{l-\text{a,b,c}}$ and line currents $i_{\text{a,b,c}}$.

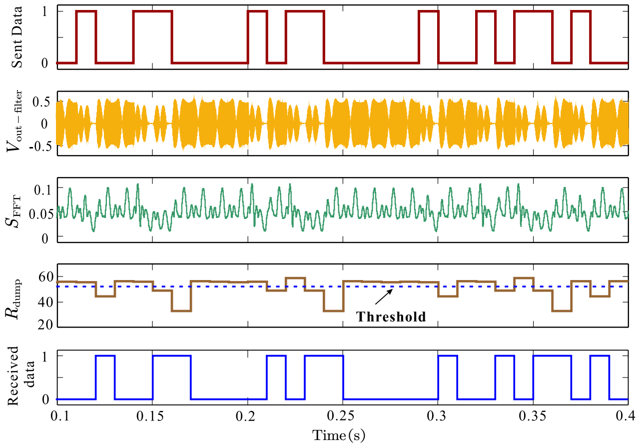

Fig. 13. Demodulation waveforms for VZVPM-based TPC.

integrate window are summed and dumped. Fig. 13 displays the waveforms of filter's output $V_{\text{out-filter}}$, the sliding FFT result $S_{\text{FFT}}$, and integrate and dump result $R_{\text{dump}}$. By interpreting the demodulated data as "0" if $R_{\text{dump}}$ is above the threshold and "1" otherwise, the data can be accurately demodulated with one bit time delay.

*3) Threshold Regulation and BER Performance:* The threshold can be chosen within a range to separate the $R_{\text{dump}}$ for bit "0" and "1" online, which can be bounds of that range. The middle of these upper and lower bounds can be a suitably chosen threshold. Fig. 14 shows threshold ranges with different $p$ as the line distance $d$ increases to 1 km. The time step is set at 0.2 $\mu$s, and the sampling rate in both the FFT and the integrate and dump module is 100 kHz. Both the threshold and its range increase as $p$ for bit "0" shifts away from 0, indicating greater robustness to noise and lower bit error rate when the absolute value of $p$ is larger. Both the threshold and its range decrease as the line distance increases. Hence, the bit error rate could be higher as the line distance increases because the upper and lower bounds get closer, making it ineffective to separate the dumped results for "0" and "1" with noise.

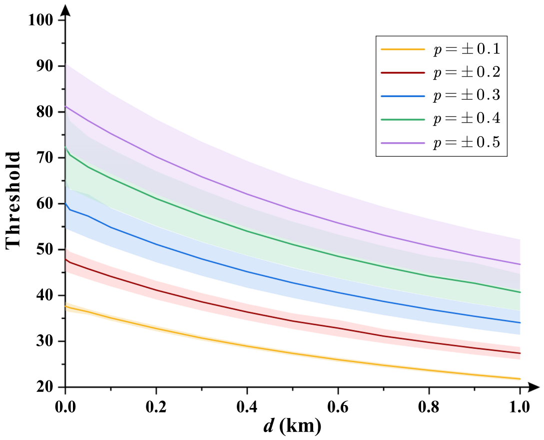

Fig. 14. Relationship diagram between threshold ranges and the line distance given diverse zero-vector positions $p$.

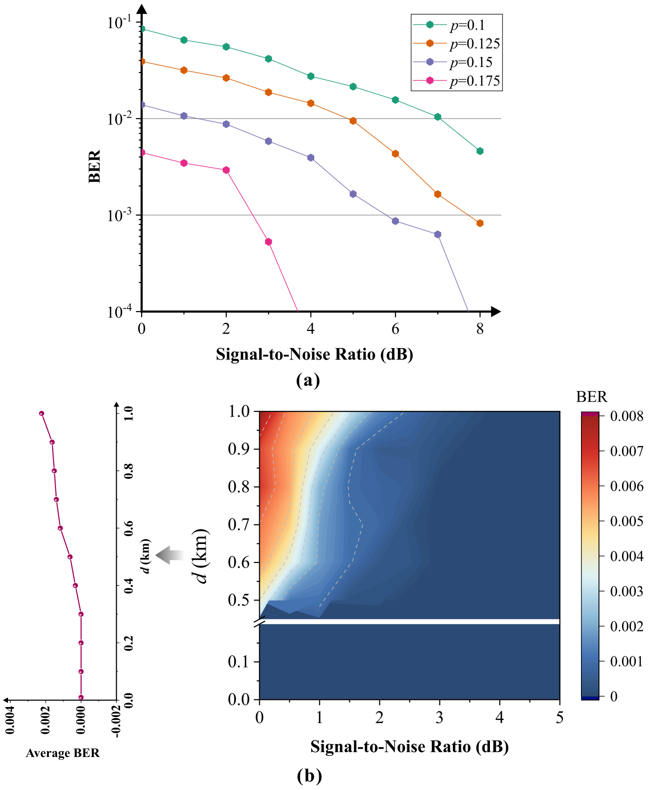

Fig. 15. Bit error rate: (a) with various zero-vector positions $p$ and (b) with increasing line distance $d$ when $p = 0.25$.

Furthermore, maintaining distance at 10 m, selecting thresholds shown in Fig. 14, considering the additive white Gaussian noise in the power line, and normalizing the input signal power (which is the switching ripple power, i.e., the sampled line-to-line voltages without the fundamental component), the BER for diverse $p$ with increasing signal-to-noise ratio (SNR) is demonstrated in Fig. 15(a). The BER increases as the zero

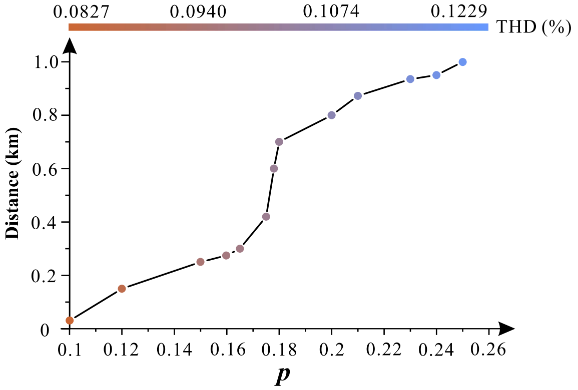

Fig. 16. Maximum achievable transmission distance under different positions of the zero vector $p$ and the THD at 10 kHz switching frequency and a maximum BER of 1%.

vector positions for bits “0” and “1” become closer, and it shows that the VZVPM TPC method can maintain a low BER level ($< 1\%$) with strong noise in most cases (SNR$<$ 8 dB). When $p > 0.25$, the BER can be less than $10^{-4}$ at a distance of 10 m. Assuming $p$=0.25, the BER with increasing line distance and SNR is measured and shown in Fig. 15(b). The average BER curve as a function of increasing line distance is also depicted. From the BER contour map and its average curve, it is obvious that the BER result is increased as the line distance increases due to the narrow threshold range at longer distance, which is consistent with the observation as shown in Fig. 14. Although the bit rate is relatively low, it is particularly useful for harsh environments, i.e. for channels with a low SNR at the receiver side.

*4) Transmission Distance and Scalability:* Long distance communication and a high bit rate are desired, but this results in a high bit error rate. As the line distance increases, the BER increases for the same SNR. It is generally acceptable that the BER should typically be less than 1%. Given an uncoded BER of 1%, the residual BER after forward error correction coding can be made arbitrarily small [27]. It is possible to limit the distance and bit rate to achieve this BER threshold. There is a tradeoff between distance, bit rate, power quality, and BER that can be dynamically turned by shifting the zero vector position $p$ to suit different application scenarios. For example, if long distance and low BER are priorities, power quality could be sacrificed slightly by shifting the zero vector position further rightward/leftward, also by reducing the bit rate with the same effect as repetition code. If good power quality and high bit rate are priorities, distance and BER could be reduced until the minimum requirements are met.

In order to ascertain the maximum transmission distance, it is necessary to first maintain a constant SNR, and gradually increase the distance and measure the BER. The distance at which the BER reaches a threshold, for instance, 1% as motivated above, can be regarded as the maximum transmission distance. As it shown in Fig. 16, the maximum transmission distance is estimated under diverse zero-vector positions $p$ and the THD, given an example with a switching frequency of 10 kHz and a noisy environment where the SNR equals 1 dB. Within the range of $p$ from 0.1 to 0.26, the THD is almost proportional to the zero-vector position $p$ according to Fig. 11, so the distance curves as the function of zero-vector position and as a function of THD are similar in Fig. 16. The transmission distance surges in the range of $p$ from 0.17 to 0.18, and exhibits a flat increase within other ranges of $p$. It should be noted that the cable parameters used and displayed in Table III pertain to a low-voltage grid. Consequently, the distance measured in Fig. 16 is constrained to 1 km. In our case study, the distance when $p$ = 0.25 could extend up to 1 km, which is sufficiently extensive to encompass a low voltage smart grid [26]. Moreover, it is not recommended to choose a value of $p$ less than 0.1 due to the short distance.

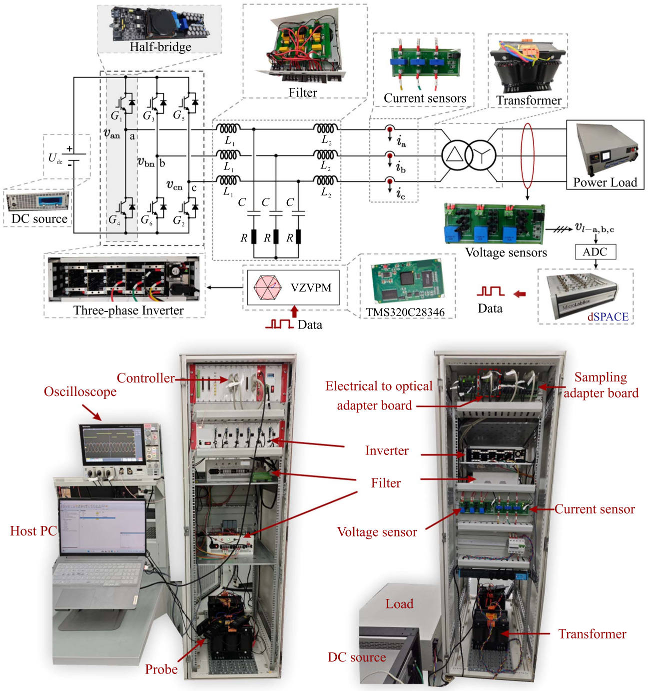

Fig. 17. Prototype of three-phase DC–AC talkative power converter.

In larger smart grid setups, where more inverters connected to renewable energy sources need to communicate at the same time, VZVPM should be combined with a multiplexing technology such as time-division or code-division multiple access. This will allow the data center to distinguish the address of data sources and receive the data. This is a possible subject for future research.

## B. Experimental Results

Our prototype is shown in Fig. 17. A delta-wye connection transformer with 1:1 turn ratio is connected between the load and the inverter for galvanic isolation. The power of the three-phase load can be selected. Its full power is 10 kW and the voltage is 220 V, so the resistance in each phase is 14.52 Ω at full load. The load power in the experiment is chosen to be 8 kW, and the resistance in each phase is 18.15 Ω. The main processor for VZVPM control is TI’s TMS320C28346, and the dead-time duration is specified as 2 $\mu$s. Gate drives for a random data sequence are shown in Fig. 18. With a time delay $T_\mathrm{d}$, which is about 0.4 times

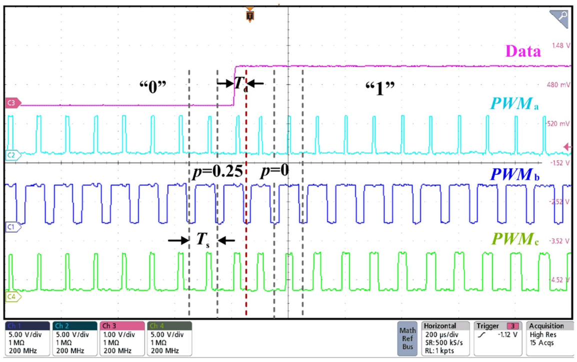

Fig. 18. Experimental waveforms of the gate drives for random bits.

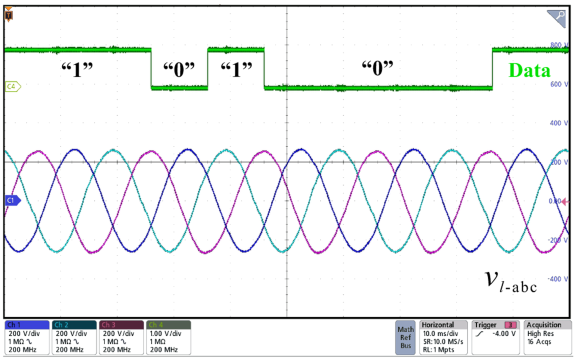

Fig. 19. Waveforms of the line-to-line voltages for random bits.

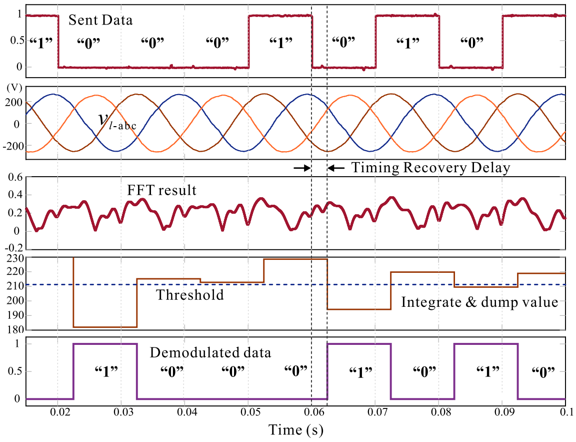

Fig. 20. Demodulation process in experiment.

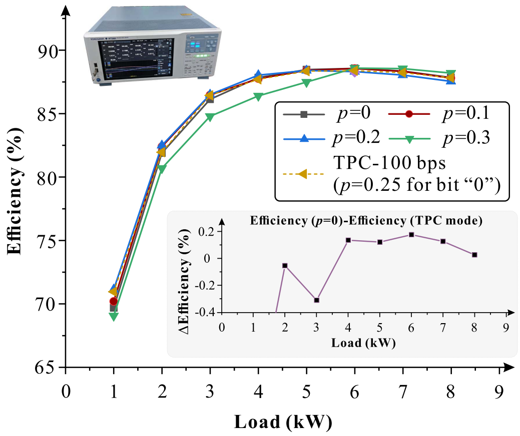

Fig. 21. Power conversion efficiency at varying load conditions and zero-vector positions $p$.

the switching period $T_s$, the pulse position shifts from the right to the center as the bit jumps from "0" to "1." Line-to-line voltages given different bits are shown in Fig. 19, and the demodulation process is shown in Fig. 20. The total time delay is equal to the timing recovery delay (0.25 b length) plus the integrate and dump delay (1 b length). Correspondingly, 100 b/s TPC with the total latency of 0.0125 s is achieved, which is close to the bound of secondary control.The power conversion efficiency curves at different load conditions and zero vector positions $p$ are measured using a YOKOGAWA WT5000 precision power analyzer, as shown in Fig. 21. For different zero vector positions $p$, the efficiencies are almost the same at 6 kW load (88.5%) and vary slightly when the load is less or greater than 6 kW. At full load (8 kW), the difference in efficiency for different zero vector positions is less than 2%. The efficiency curve in TPC mode is also measured. In our TPC mode, the bit rate is 100 b/s and the zero vector position $p$ jumps between 0 and 0.25 for bit "1" and "0," respectively, according to the data sequence with equal probability of bit "0" and "1." In order to demonstrate the impact of VZVPM-based TPC on efficiency, the efficiency deviation is rendered smaller and is presented in Fig. 21. The efficiency deviation is defined as the efficiency when $p = 0$ minus the efficiency in TPC mode, which is within $-0.3\%$ and 0.2%, indicating that the VZVPM-TPC approach has minor impact on the efficiency.

## V. CONCLUSION

In this study, VZVPM has been proposed to realize TPC for a three-phase dc–ac converter with a bit rate of 100 b/s at 10 kHz switching frequency, i.e., the switching frequency utilization rate equals 0.01. The harmonic characteristics have been analyzed, which proves that the amplitude of some targeted harmonics has relationships with the position of the zero vector. The average THD is 0.1295%, and the variation of THD is negligible (0.052%) in TPC mode. The bit rate is determined by the resolution of the target frequencies, which could be optimized based on harmonic characteristics. Accordingly, the transmitted data can be extended to 1 km and demodulated with a latency of 0.0125 s using the sliding FFT approach. The bit error rate is low ($< 0.3\%$) as $p$ drifts away from 0, and becomes higher as the line distance increases due to the narrowing of the threshold range. Simulations and experiments confirm the feasibility of VZVPM-based TPC, and the robustness to noises and dead time. The efficiency difference is within 2% under different zero vector positions at full load and the efficiency is less affected by VZVPM TPC. Details on bit-rate optimization, communication delay reduction, and the mechanism of channel influence on TPC are subjects of future work.

## REFERENCES

[1] V. C. Gungor et al., “A survey on smart grid potential applications and communication requirements,” *IEEE Trans. Ind. Informat.*, vol. 9, no. 1, pp. 28–42, Feb. 2013.

[2] L. Lampe, A. M. Tonello, and T. G. Swart, *Power Line Communications: Principles, Standards and Applications From Multimedia to Smart Grid*. Hoboken, NJ, USA: John, 2016.

[3] W. Stefanutti, S. Saggini, P. Mattavelli, and M. Ghioni, “Power line communication in digitally controlled DC–DC converters using switching frequency modulation,” *IEEE Trans. Ind. Electron.*, vol. 55, no. 4, pp. 1509–1518, Apr. 2008.

[4] X. He, R. Wang, J. Wu, and W. Li, “Nature of power electronics and integration of power conversion with communication for talkative power,” *Nature Commun.*, vol. 11, no. 1, pp. 1–12, 2020.

[5] M. Angjelichinoski, Č. Stefanović, P. Popovski, H. Liu, P. C. Loh, and F. Blaabjerg, “Multiuser communication through power talk in DC microgrids,” *IEEE J. Sel. Areas Commun.*, vol. 34, no. 7, pp. 2006–2021, Jul. 2016.

[6] M. Liserre, H. Beiranvand, Y. Leng, R. Zhu, and P. A. Hoeher, “Overview of talkative power conversion technologies,” *IEEE Open J. Power Electron.*, vol. 4, pp. 67–80, Jan. 2023.

[7] Y. Leng, D. Yu, K. Han, S. S. Yu, and Y. Hu, “OFDM-based intrinsically safe power and signal synchronous transmission for CC-PT-controlled buck converters,” *IEEE Trans. Power Electron.*, vol. 37, no. 9, pp. 10319–10331, Sep. 2022.

[8] F. Wang, D. Yuan, and X. Zhang, “Low-voltage inbound power-line communication based on talkative power conversion,” *IEEE J. Emerg. Sel. Topics Power Electron.*, vol. 12, no. 4, pp. 3348–3359, Aug. 2024.

[9] Y. Guan, J. Wu, K. Liu, K. Zhao, and X. He, “Multiinput PV optimizer system with built-in communication using talkative power conversion,” *IEEE J. Emerg. Sel. Topics Power Electron.*, vol. 12, no. 4, pp. 3392–3401, Aug. 2024.

[10] P. A. Hoeher, M. Mewis, and M. Liserre, “Channel coding and receiver design for simultaneous wireline information and power transfer,” *IEEE Open J. Power Electron.*, vol. 2, pp. 545–558, Oct. 2021.

[11] K. Liu, Y. Hui, J. Chen, J. Wu, and X. He, “Simultaneous power and data modulation scheme for LLC resonant converter,” *IEEE Trans. Power Electron.*, vol. 39, no. 1, pp. 270–279, Jan. 2024.

[12] K. Liu, H. Yang, Y. Chen, Y. Hui, J. Wu, and X. He, “Active rectified LLC resonant converter using combined frequency and phase modulation for talkative power conversion,” *IEEE J. Emerg. Sel. Topics Power Electron.*, vol. 12, no. 4, pp. 3315–3324, Aug. 2024.

[13] Y. Hui, R. Zhang, J. Wu, C. Ren, R. Wang, and X. He, “Embedding data signals into power control loop of inverters for power line communication in AC microgrids,” in *Proc. 5th IEEE Conf. Energy Internet Energy Syst. Integration*, 2021, pp. 763–767.

[14] L. Zheng et al., “Research on channel characteristics of energy-information integrated AC transmission system,” *IEEE J. Emerg. Sel. Topics Power Electron.*, to be published, doi: 10.1109/JESTPE.2024.3483837.

[15] H. Liu, Y. Leng, and D. Yu, “Power & signal synchronous transmission strategy for three-phase voltage source inverter,” in *Proc. Conf. Int. Joint Conf. Energy, Elect. Power Eng.*, 2022, vol. 899, pp. 145–153.

[16] Y. Zhang, G. Chen, Y. Hu, C. Gong, and Y. Wang, “Cascaded multilevel inverter based power and signal multiplex transmission for electric vehicles,” *CES Trans. Elect. Mach. Syst.*, vol. 4, no. 2, pp. 123–129, 2020.

[17] S. Shan and L. Umanand, “A novel fractional harmonic $d-q$ domain based power line signaling technique for power converters in a microgrid,” *IEEE Trans. Power Electron.*, vol. 34, no. 11, pp. 11264–11277, Nov. 2019.

[18] Z. Wang, D. Zhou, X. Liu, Z. Shen, and J. Zou, “Sideband harmonic-based talkative power conversion,” *IEEE Trans. Power Electron.*, vol. 39, no. 10, pp. 13708–13719, Oct. 2024.

[19] Y. Yan, Y. Qian, H. Sharif, and D. Tipper, “A survey on smart grid communication infrastructures: Motivations, requirements and challenges,” *IEEE Commun. Surveys Tuts.*, vol. 15, no. 1, pp. 5–20, First Quarter 2013.

[20] S. Liu, X. Wang, and P. X. Liu, “Impact of communication delays on secondary frequency control in an islanded microgrid,” *IEEE Trans. Ind. Electron.*, vol. 62, no. 4, pp. 2021–2031, Apr. 2015.

[21] I. Serban, S. Céspedes, C. Marinescu, C. A. Azurdia-Meza, J. S. Gómez, and D. S. Hueichapan, “Communication requirements in microgrids: A practical survey,” *IEEE Access*, vol. 8, pp. 47694–47712, 2020.

[22] H. Yan, J. Yang, and F. Zeng, “Three-phase current reconstruction for PMSM drive with modified twelve sector space vector pulse width modulation,” *IEEE Trans. Power Electron.*, vol. 37, no. 12, pp. 15209–15220, Dec. 2022.

[23] Y. Leng, R. Zhu, M. Liserre, P. A. Hoeher, and H. Beiranvand, “SVPWM-based three-phase DC/AC talkative power converters,” in *Proc. IEEE 49th Annu. Conf. IEEE Ind. Electron. Soc.*, Singapore, 2023, pp. 1–6.

[24] Y. Leng, R. Zhu, M. Liserre, and P. A. Hoeher, “Variable zero-vector-width-based three-phase DC/AC talkative power conversion,” *IEEE J. Emerg. Sel. Topics Power Electron.*, vol. 12, no. 4, pp. 3402–3414, Aug. 2024.

[25] D. G. Holmes and T. A. Lipo, *Pulse Width Modulation for Power Converters: Principles and Practice*. Hoboken, NJ, USA: Wiley, 2003.

[26] S. Papathanassiou, N. Hatziargyriou, and K. Strunz, “A benchmark low voltage microgrid network,” in *Proc. CIGRE Symp.: Power Syst. Dispersed Gener.*, 2005, vol. 1, pp. 1–8.

[27] S. Lin and J. Li, *Fundamentals of Classical and Modern Error-Correcting Codes*. Cambridge, U.K.: Cambridge Univ. Press, 2021.

**Yang Leng** (Student Member, IEEE) received the B.S. degree in electrical engineering from the School of Electrical Engineering and Its Automation, Henan Polytechnic University, Jiaozuo, China, in 2018, and the M.S. degree in electrical engineering from the School of Electrical and Power Engineering, China University of Mining and Technology, Xuzhou, China, in 2021. He is currently working toward the Ph.D. degree in energy and power technology with the Department of Electrical Engineering, Harbin Institute of Technology, Shenzhen, China.

His research interests include talkative power conversion, nonlinear dynamics, and electromagnetic compatibility.

Dr. Leng is currently a Reviewer for IEEE TRANSACTIONS ON POWER ELECTRONICS, IEEE TRANSACTIONS ON INDUSTRIAL ELECTRONICS, IEEE JOURNAL OF EMERGING AND SELECTED TOPICS IN POWER ELECTRONICS, IEEE TRANSACTIONS ON CIRCUITS AND SYSTEMS I: REGULAR PAPERS, and IEEE OPEN JOURNAL OF POWER ELECTRONICS.

**Rongwu Zhu** (Senior Member, IEEE) received the B.Eng. degree in electrical engineering from Nanjing Normal University, Nanjing, China, in 2007, and the Ph.D. degree in energy technology from the Department of Energy Technology, Aalborg University, Aalborg, Denmark, in 2015.

From 2011 to 2012, he was a Guest Researcher with Aalborg University. From 2016 to 2021, he was a group leader of renewable power grid and Senior Researcher with the Chair of Power Electronics, Christian-Albrechts University of Kiel, Kiel, Germany. He is currently a Full Professor, Director of Department of Electrical Engineering, and Vice Dean of School of Robotics and Advanced Manufacturing with the Harbin Institute of Technology, Shenzhen, China. He is also a Director of the HITsz-CYGsr joint lab of modern distribution power system and intelligent equipment. He has authored and coauthored around 140 technical papers (more than 1/3 of them in international peer-reviewed journals/magazine), one book chapter, and 25 granted or pending patents. His research interests include advanced control and grid integration of renewable energy resources, autonomous control renewables-dominated grids, AI technology for power electronics and electricity grids, and digitalization and talkative power conversion.

Dr. Zhu was the recipient of the third prize of the “Data Element-x” national competition 2024. He was the Editor of the *International Transactions on Electrical Energy System*, an Associate Editor for *Renewable Power Generation*, Associate Editor for IEEE OPEN JOURNAL OF POWER ELECTRONICS, and a Guest Associate Editor for the IEEE JOURNAL OF EMERGING AND SELECTED TOPICS IN POWER ELECTRONICS, the Guest Editor-in-Chief of the *CSEE Journal of Power and Energy Systems*, and Technical Committee Chair and a Member for several International Conferences.

**Peter Adam Hoeher** (Fellow, IEEE) received the Dipl.-Ing. degree in electrical engineering from RWTH Aachen University, Aachen, Germany, in 1986, and the Dr.-Ing. degree in electrical engineering from the University of Kaiserslautern, Kaiserslautern, Germany, in 1990.

From 1986 to 1998, he was with the German Aerospace Center (DLR), Oberpfaffenhofen, Germany. From 1991 to 1992, he was on leave at AT&T Bell Laboratories, Murray Hill, NJ, USA. In 1998, he joined the University of Kiel, Kiel, Germany, where he is currently a Full Professor of Electrical and Information Engineering. He has supervised more than 20 doctoral and 230 bachelor's or master's theses, authored or coauthored about 350 peer-reviewed conference and journal papers with a total of more than 16 000 citations, has written two textbooks, and was granted about 20 patent families. His research interests are on digital communications with focus on wireless communication, visible light communication, and simultaneous information and power transfer.

**Marco Liserre** (Fellow, IEEE) received the M.Sc. and Ph.D. degrees in electrical engineering from the Politecnico di Bari, Bari, Italy, in 1998 and 2002, respectively.

He has been an Associate Professor with the Politecnico di Bari and, since 2012, a Professor of Reliable Power Electronics with Aalborg University, Aalborg, Denmark. Since 2013, he has been a Full Professor and holds the Chair of Power Electronics with the University of Kiel, Kiel, Germany. He has been offered and declined professorships at several universities. He has authored or coauthored more than 700 technical papers (1/3 of them in international refereed journals), one book, and seven granted patents (four with companies). These works have earned more than 50 000 citations.

Dr. Liserre was selected as an Highly Cited Researcher in the field of Engineering (Clarivate Web of Science) from 2014 to 2021. Several of his students (M.Sc., Ph.D., and postdocs) are in leading positions in industry and universities worldwide. In 2023, he joined the Fraunhofer ISIT on a part-time basis as deputy Director and Director of the new division "Electronic Energy Systems," as well as of the Kiel branch of the Fraunhofer ISIT. Since 2025, he has been an acting Director of Fraunhofer ISIT. He is a member of IAS, IEEE Power Electronics Society (PELS), IEEE Power and Energy Society, and IEEE Industrial Electronics Society (IES). He has served all these societies in various capacities. In PELS, he is Co-Editor of the *IEEE Open Access Journal in Power Electronics* and Technical Committee Chairman of the Committee on Electronic Power Grid Systems. He has co-chaired several IEEE conferences being several times Chairman. He was the recipient of 16 awards from IEEE, PCIM, and EPE-PEMC, including the prestigious 2018 IEEE-IES Mittelmann Achievement Award and the 2023 IEEE-PELS R. David Middlebrook Achievement Award. In 2023, he was also the recipient of the title of "Ufficiale" by the President of the Italian Republic. In 2025, he will be a Chairman of Powertech 2025 in Kiel.